Commun. Comput. Phys.
doi: 10.4208/cicp.171011.180712a

Vol. **14**, No. 1, pp. 126-152
July 2013

A Lattice Boltzmann and Immersed Boundary Scheme for Model Blood Flow in Constricted Pipes: Part 1 – Steady Flow

S. C. Fu*, W. W. F. Leung and R. M. C. So

Department of Mechanical Engineering, The Hong Kong Polytechnic University, Hung Hom, Hong Kong.

Received 17 October 2011; Accepted (in revised version) 18 July 2012

Communicated by Kazuo Aoki

Available online 30 October 2012

Abstract. Hemodynamics is a complex problem with several distinct characteristics; fluid is non-Newtonian, flow is pulsatile in nature, flow is three-dimensional due to cholesterol/plague built up, and blood vessel wall is elastic. In order to simulate this type of flows accurately, any proposed numerical scheme has to be able to replicate these characteristics correctly, efficiently, as well as individually and collectively. Since the equations of the finite difference lattice Boltzmann method (FDLBM) are hyperbolic, and can be solved using Cartesian grids locally, explicitly and efficiently on parallel computers, a program of study to develop a viable FDLBM numerical scheme that can mimic these characteristics individually in any model blood flow problem was initiated. The present objective is to first develop a steady FDLBM with an immersed boundary (IB) method to model blood flow in stenoic artery over a range of Reynolds numbers. The resulting equations in the FDLBM/IB numerical scheme can still be solved using Cartesian grids; thus, changing complex artery geometry can be treated without resorting to grid generation. The FDLBM/IB numerical scheme is validated against known data and is then used to study Newtonian and non-Newtonian fluid flow through constricted tubes. The investigation aims to gain insight into the constricted flow behavior and the non-Newtonian fluid effect on this behavior.

AMS subject classifications: 76Z05, 76M20, 65N06

Key words: Finite difference method, lattice Boltzmann method, immersed boundary method, blood flow, constricted pipe.

1 Introduction

Flow behavior in a stenosed artery is quite different from that in normal ones. Viscous stresses and resistance to flow are much higher in stenosed arteries compared to their

*Corresponding author. *Email addresses:* mescfu@ust.hk (S. C. Fu), Wallace.Leung@inet.polyu.edu.hk (W. W. F. Leung), mmmcso@polyu.edu.hk (R. M. C. So)

normal counterparts. If the stenosis is severe enough, high blood flow speeding through narrow stenosis will give rise to considerable compressive stress in the tube wall, and critical flow conditions such as negative pressure, high shear stress and flow separation will develop. These flow and mechanical conditions can cause artery fatigue, arterial compression flow limitation, and possible flow-induced instabilities. The resulting static and dynamic loading on the diseased arterial wall may be sufficiently vigorous or sustained to fracture the plaque cap of the stenosis, thus causing fragments to sweep downstream. This process could directly lead to serious clinical consequences, such as strokes or heart attacks [1–3]. In view of this rather complicated and complex flow behavior, any numerical scheme used to investigate hemodynamics should at least be able to handle pulsating flow of Newtonian and non-Newtonian fluids through three-dimensional (3-D) tubes with and without constrictions where the boundary geometry changes with time, and with solid and/or elastic boundaries.

Lattice Boltzmann method (LBM) has developed into an alternative powerful numerical solver for the Navier-Stokes (NS) equations and for modeling flow physics [4–6]. The equation is hyperbolic and can be solved locally, explicitly, and efficiently on parallel computers [7, 8]. Consequently, the applicability and suitability of LBM to the field of blood flow has been widely explored by researchers [7–14]. Real arterial stenoses rarely have well-defined geometric shapes and stenotic plaques usually have complex geometries. Therefore, it is difficult to apply the boundary conforming grid method to such problems. Besides, the plague built up boundary could be changing with time. The complicated body-fitted geometry method plays a significant role in numerical stability and its eventual accuracy. Hence, for most simulations, either the grids were generated a priori [12], or the computer generated meshes were checked manually to ensure sufficient accuracy of the computational results [13]. In the case of a generated mesh, an a priori knowledge of the artery configuration is required. Therefore, for model blood flow problem, it would be desirable to develop a numerical technique that does not necessarily keeps the mesh conforms to the complicated boundary. One such technique is the immersed boundary (IB) method first introduced by Peskin [15] in his study of blood flow in the human heart. In the IB method, the governing equations are discretized on a fixed Cartesian grid. The wall conditions of a boundary are accounted for by introducing an external force field in the equations of motion, which is designed to ensure that the fluid satisfies the no-slip condition on blood vessel walls. The boundary was modelled as a set of elements linked by springs. Subsequent advanced boundary treatments dealing with complex geometry, moving boundary and even fluid-structure interaction (FSI) can be derived from the IB method [16].

Recently, Fu et al. [17,18] have developed a finite difference lattice Boltzmann method (hereafter designated as FDLBM) that provides a convenient algorithm for setting the boundary condition using a splitting method to solve the discrete lattice Boltzmann (LB) equation. Their FDLBM is capable of simulating flows of Newtonian and non-Newtonian fluids, with (or without) external body forces [17]. Also, the inherent compressibility effect of the conventional LBM [19], which might produce significant errors in some incom-

pressible flow simulations, is eliminated [18]. Through this numerical approach, a wide variety of governing equations can be similarly treated [20]. The work of Fu et al. [17] was originally aimed at the simulation of micro-channel flows, but its application can be much broader [20]. However, solution of the FDLBM relies on Cartesian grids; hence, it is not easily adapted to flows with complex boundary geometries. This is a serious drawback of the FDLBM. If this FDLBM were to be a viable tool for blood flow simulations, implementing the IB method into the FDLBM would give rise to a numerical tool that could handle complex boundaries using Cartesian grids in axisymmetric and 3-D flow. Therefore, the first objective of this paper is to implement the IB into the FDLBM; this new tool is designated as the FDLBM/IB numerical scheme.

The present paper reports on the development of the FDLBM/IB scheme. After validating the scheme, numerical simulations of Newtonian and non-Newtonian fluid flow in constricted tubes are investigated and discussed. There is increasing evidence that hemodynamics is closely related to intimal thickening, lipid deposition and endothelial adaptations, cell adhesion, elongation, and adaptation, thrombus development, and various cell behaviour under specific shear stress conditions. Consequently, blood pressure and wall stress have considerable effects on artery remodelling [1–3]. In view of this, the second objective of this paper is to investigate hemodynamic in stenotic arteries by deducing scaling laws for pressure drop and wall shear stress in constricted tubes using the simulated results.

2 Finite difference lattice Boltzmann method

Details of the governing NS and the LB equations for steady incompressible flows have been given in earlier work [17, 18, 20]. In view of this, only a brief description of these equations is reported here. In the following, the NS equations and its associated boundary conditions are described first; it is then followed by a brief discussion of the LB equation and the FDLBM.

2.1 Navier-Stokes equations and boundary conditions

A schematic representation of the present problem is shown in Fig. 1. An incompressible steady flow passes through a rigid tube with a localized constriction. The effect of swirl in the flow is not considered and the problem, even with the presence of secondary flow behind the constriction, is assumed to be axisymmetric. The flow upstream and downstream of the constriction is assumed to be a fully developed Poiseuille flow. The unconstricted radius of the tube is $\hat{R}_0$ and the maximum upstream velocity $\hat{U}_0$ is taken to be the centerline velocity. Hence, the through flow rate is $\hat{Q}=\pi\hat{R}_0^2\hat{U}_0/2$ and the Reynolds number is defined as $Re=\hat{\rho}_0\hat{U}_0\hat{R}_0/\hat{\mu}_0$. All equations given below are dimensionless and the following normalization is utilized,

$$(x,y)=\frac{(\hat{x},\hat{y})}{\hat{R}_0},\qquad (u,v)=\frac{(\hat{u},\hat{v})}{\hat{U}_0},\qquad \rho=\frac{\hat{\rho}}{\hat{\rho}_0},\qquad \mu=\frac{\hat{\mu}}{\hat{\mu}_0},\qquad p=\frac{\hat{p}}{\hat{\rho}_0\hat{U}_0^2}, \tag{2.1}$$

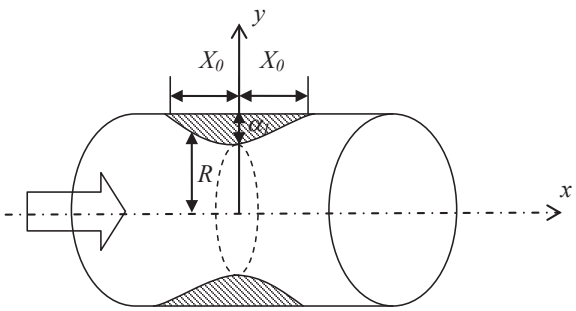

Figure 1: Schematic of the model blood flow problem investigated.

where (x,y) are respectively the axial and radial coordinates, (u,v) are the axial and radial velocity components along x and y, respectively, ρ is fluid density, μ is fluid dynamic viscosity, and p is pressure. Without loss of generality, ρ is taken to be unity in an incompressible flow. However, in the following presentation, ρ is kept in the equations for convenience. Their corresponding dimensional quantities are represented by a 'hat'. In cylindrical coordinates, the NS equations can be written as

$$\frac{\partial u}{\partial x}+\frac{\partial v}{\partial y}+\frac{v}{y}=0, \tag{2.2a}$$

$$\rho\left(\frac{\partial u^2}{\partial x}+\frac{\partial uv}{\partial y}+\frac{uv}{y}\right)=-\frac{\partial p}{\partial x}+\frac{\partial \tau_{xx}}{\partial x}+\frac{\partial \tau_{xy}}{\partial y}+\frac{\tau_{xy}}{y}, \tag{2.2b}$$

$$\rho\left(\frac{\partial uv}{\partial x}+\frac{\partial u^2}{\partial y}+\frac{v^2}{y}\right)=-\frac{\partial p}{\partial y}+\frac{\partial \tau_{xy}}{\partial x}+\frac{\partial \tau_{yy}}{\partial y}+\frac{\tau_{yy}}{y}, \tag{2.2c}$$

where the shear stress components have been normalized by $\hat{\rho}_0\hat{U}_0^2$ and are defined by

$$\tau_{xx}=\frac{2}{\mathrm{Re}}\frac{\partial u}{\partial x},\qquad \tau_{yy}=\frac{2}{\mathrm{Re}}\frac{\partial v}{\partial y},\qquad \tau_{xy}=\frac{1}{\mathrm{Re}}\left(\frac{\partial u}{\partial y}+\frac{\partial v}{\partial x}\right). \tag{2.3}$$

The upstream and downstream condition is assumed to be a fully developed Poiseuille flow; therefore, the velocity profiles are

$$\begin{cases} u=1-y^2, \\ v=0, \end{cases}\qquad x\to\pm\infty. \tag{2.4}$$

The geometry of the constriction is described by a cosine curve, just as that assumed by previous researchers [21,22],

$$R(x)=1-\frac{\alpha_1}{2}\left[1+\cos\left(\frac{\pi x}{X_0}\right)\right],\qquad -X_0\le x\le X_0, \tag{2.5a}$$

$$R(x)=1,\qquad |x|\ge X_0, \tag{2.5b}$$

where α_1 and X_0 are constants used to characterize the length and degree of occlusion.

2.2 Brief description of the FDLBM

The FDLBM of [17,18] proposed to consider the NS equations in cylindrical coordinates as a conservative set plus additional source terms; here this same approach is adopted. Basically, the FDLBM [17] solves the BGK-type modeled lattice Boltzmann equation,

$$\frac{\partial f_\alpha}{\partial t}+\vec{\xi}_\alpha\cdot\nabla_{\vec{x}}f_\alpha+g_\alpha=-\frac{1}{\varphi}(f_\alpha-f_\alpha{}^{eq}), \tag{2.6}$$

using a splitting method. All distribution functions including the equilibrium distribution function f_α^{eq} in Eq. (2.6) are normalized by $\hat{\rho}_0$, e.g. $f_\alpha=\hat{f}_\alpha/\hat{\rho}_0$. Besides the basic distribution function f_α, which is used to recover the conservative set of NS equations, another distribution function g_α is added to help recover the source terms in Eqs. (2.2a)-(2.2c). These source terms arise as a result of writing the NS equations for the constricted tube problem in cylindrical coordinates. The lattice model employed is a D2Q9 model with lattice velocities $\vec{\xi}_\alpha=(\xi_{\alpha x},\xi_{\alpha y})$ given by

$$\vec{\xi}_0=0, \qquad \alpha=0, \tag{2.7a}$$
$$\vec{\xi}_\alpha=\sigma(\cos[\pi(\alpha-1)/4],\ \sin[\pi(\alpha-1)/4]), \qquad \alpha=1,3,5,7, \tag{2.7b}$$
$$\vec{\xi}_\alpha=\sqrt{2}\sigma(\cos[\pi(\alpha-1)/4],\ \sin[\pi(\alpha-1)/4]), \qquad \alpha=2,4,6,8, \tag{2.7c}$$

where σ is a numerical parameter to be determined later. In Eq. (2.6), the f_α^{eq} is defined as

$$f_\alpha^{eq}=A_\alpha+\xi_{\alpha x}Ax_\alpha+\xi_{\alpha y}Ay_\alpha+\xi_{\alpha x}^2Bxx_\alpha+\xi_{\alpha y}^2Byy_\alpha+\xi_{\alpha x}\xi_{\alpha y}Bxy_\alpha, \tag{2.8}$$

and the coefficients can be determined as

$$A_0=\rho-\frac{2p}{\sigma^2}-\frac{\rho|\vec{u}|^2}{\sigma^2}+\frac{\tau_{xx}+\tau_{yy}}{\sigma^2}, \qquad A_1=A_2=0, \tag{2.9a}$$
$$Ax_1=\frac{\rho u}{2\sigma^2}, \qquad Ax_2=0, \tag{2.9b}$$
$$Ay_1=\frac{\rho v}{2\sigma^2}, \qquad Ay_2=0, \tag{2.9c}$$
$$Bxx_1=\frac{1}{2\sigma^4}\left(p+\rho u^2-\tau_{xx}\right), \qquad Bxx_2=0, \tag{2.9d}$$
$$Byy_1=\frac{1}{2\sigma^4}\left(p+\rho v^2-\tau_{yy}\right), \qquad Byy_2=0, \tag{2.9e}$$
$$Bxy_2=\frac{1}{4\sigma^4}\left(\rho uv-\tau_{xy}\right), \qquad Bxy_1=0. \tag{2.9f}$$

The shear stress components, τ_{xx}, τ_{yy}, τ_{xy}, are found by using a central difference scheme. If a Newtonian fluid is assumed, Eq. (2.3) with constant μ is adopted for the stress components. However, it is clear that other non-Newtonian fluid models can also be assumed.

The additional distribution function g_α and the associated coefficients are given by (e.g. see [17])

$$g_\alpha = A_\alpha + \xi_{\alpha x} A x_\alpha + \xi_{\alpha y} A y_\alpha, \tag{2.10a}$$

$$A_0 = 0, \qquad A_1 = \frac{\rho v}{4y}, \qquad A_2 = 0, \tag{2.10b}$$

$$A x_1 = \frac{1}{2\sigma^2 y}\left(\rho uv - \tau_{xy}\right), \qquad A x_2 = 0, \tag{2.10c}$$

$$A y_1 = \frac{1}{2\sigma^2 y}\left(\rho v^2 - \tau_{yy}\right), \qquad A y_2 = 0, \tag{2.10d}$$

so that the following constraints are fulfilled for the distribution function g_α,

$$\sum_{\alpha=0}^{8} g_\alpha = \frac{\rho v}{y}, \qquad \sum_{\alpha=0}^{8} g_\alpha \xi_{\alpha x} = \frac{\rho uv}{y} - \frac{\tau_{xy}}{y}, \tag{2.11a}$$

$$\sum_{\alpha=0}^{8} g_\alpha \xi_{\alpha y} = \frac{\rho v^2}{y} - \frac{\tau_{yy}}{y}, \qquad \sum_{\alpha=0}^{8} g_\alpha \left(\xi_{\alpha x}^2 + \xi_{\alpha y}^2\right) = 0. \tag{2.11b}$$

Finally, the macroscopic variables are determined from

$$u = \frac{1}{\rho}\sum_{\alpha=0}^{8} f_\alpha \xi_{\alpha x}, \qquad v = \frac{1}{\rho}\sum_{\alpha=0}^{8} f_\alpha \xi_{\alpha y}, \tag{2.12a}$$

$$p = \sum_{\alpha=0}^{8} f_\alpha \frac{1}{2}\left(\xi_{\alpha x}^2 + \xi_{\alpha y}^2\right) - \frac{1}{2}\rho\left(u^2 + v^2\right) + \frac{\tau_{xx} + \tau_{yy}}{2}. \tag{2.12b}$$

Numerically, Eqs. (2.6)-(2.12) are solved by a splitting method outlined below.

The initial step is to solve Eq. (2.6), by first setting its right hand side (RHS) to zero, using any numerical solver. In this paper, the Lax-Wendroff scheme is chosen for the discretization of the advective term because it is second order accurate. Also, it solves the equation locally and explicitly, and the finite difference calculation only requires information from adjacent points. The macroscopic variables are then determined using Eq. (2.12) and the boundary condition is set in macroscopic level at this moment. After obtaining a solution in this first step, it is used as the initial condition to solve the following differential equation

$$\frac{\partial f_\alpha}{\partial t} = -\frac{1}{\varphi}(f_\alpha - {f_\alpha}^{eq}). \tag{2.13}$$

These two steps together combine to give a solution to Eq. (2.6). An important procedure of the FDLBM is the application of the Euler method to Eq. (2.13), and the setting of $\varphi = \Delta t$. This procedure gives rise to exactly the same f_α before and after this time step [17,18]. Thus, no computational resource is required in this time step and the macroscopic

quantities obtained, including the boundary setting, are in fact the same as before. The procedure, therefore, allows the boundary conditions to be set at the macroscopic level, contrary to the conventional LBM which requires the boundary conditions to be set at the microscopic level. Consequently, the boundary setting can be achieved as conveniently as any conventional finite difference methods used to solve the NS equations.

The scheme is designed for steady flow, so the time variable in the equations is considered as a pseudo-time and the previous two procedures are repeated and iterated upon the pseudo-time until the following criterion is satisfied,

$$\max\left\|\partial\left(p+\frac{1}{2}\rho\left(u^2+v^2\right)-\frac{\tau_{xx}+\tau_{yy}}{2}\right)\right\|\leq\frac{\Delta t^2\sigma^2}{2}, \tag{2.14}$$

thus ensuring that the continuity equation is satisfied to an error of $\mathcal{O}(\Delta t)$. The operator '∂' denotes the difference between successive time steps and the maximum norm is taken within the whole spatial domain. Using the Lax-Wendroff scheme for the discretization of the advective term gives an overall accuracy of the numerical method as second order in space and first order in time. Since the scheme is designed for steady flow, iterations are carried out until all time derivative terms vanish, the numerical parameter σ is allowed to vary for each iteration step according to

$$\sigma=c\sqrt{\max\left\|u^2+v^2+\frac{2p-\tau_{xx}-\tau_{yy}}{\rho}\right\|}. \tag{2.15}$$

Numerical experiments (e.g. see [23]) show that better accuracy and convergence is obtained by using a time varying σ instead of a constant one. The numerical parameter σ plays an important role in the stability condition. The detailed numerical analysis can be found in [23]. The scheme will become unstable if the choice of the scaling parameter c is too small; however, it affects the convergence and accuracy if c is too large; therefore, a small enough c for stable calculation is required for all simulation cases attempted in this paper.

3 FDLBM/IB numerical scheme

The term "immersed boundary method" was first used in reference to a method developed by Peskin [15] to simulate cardiac mechanics and associated blood flow. It was used to solve the NS equations in the presence of moving immersed boundaries (the heart-valve leaflets) which moved at the local fluid velocity and exerted forces locally on the fluid. The entire simulation could be carried out on a Cartesian grid, which did not conform to the geometry of the heart, and a novel procedure was formulated to impose the effect of the immersed boundary on the flow. Due to the potential of the IB method in handling complex boundary geometries, moving and even elastic boundaries [16], it

is chosen as the tool of choice for the present simulation of flow through a pipe with constriction. The boundary inside the computational domain is called the immersed boundary. The IB is represented by a set of massless points, $\vec{X}_k=(X_k,Y_k)$ with index $k=1,\cdots,N$ that moves with the local fluid velocity $\vec{u}=(u,v)$. Hence, the tracking is Lagrangian in nature,

$$\frac{\partial \vec{X}_k}{\partial t}=\vec{u}\left(\vec{X}_k,t\right). \tag{3.1}$$

In this paper, the Euler method is used to solve the above equation; thus, the local fluid velocity is

$$\vec{u}\left(\vec{X}_k,t\right)=\int\limits_{\vec{x}\in\Omega}\vec{u}(\vec{x},t)\delta\left(\left|\vec{x}-\vec{X}_k\right|\right), \tag{3.2}$$

where δ is the Dirac delta function. It appears as a kernel in each of the equations in which a transition is made from boundary to fluid quantities or vice versa. In the present study, the original discrete delta function used by Peskin [15] is adopted. It should be noted that the choice of the discrete delta function may affect the accuracy for different types of governing equations [24]. Since satisfactory results are obtained by using Peskin's choice, it is adopted for all simulations in this paper. The effect of the immersed boundary on the surrounding fluid is transmitted through a localized forcing term $\vec{F}^{ib}=\left(F_x^{ib},F_y^{ib}\right)$, which is added as a body force in the momentum equations. This force is given by

$$\vec{F}^{ib}(\vec{x},t)=\frac{1}{N}\sum_{k=1}^{N}\vec{F}_k(t)\delta\left(\left|\vec{x}-\vec{X}_k\right|\right). \tag{3.3}$$

The relation between $\vec{X}_k$ and $\vec{F}_k$ depends on the material properties of the immersed boundary. In this paper, the immersed boundary is considered as a rigid wall, which is simulated using the mechanism employed in [24, 25]. The immersed boundary points $\vec{X}_k$ are supposed to be attached to a fictitious fixed equilibrium location $\vec{X}_k^e$ by a spring with the restoring force $\vec{F}_k$ given by

$$\vec{F}_k(t)=-\kappa\left(\vec{X}_k(t)-\vec{X}_k^e\right), \tag{3.4}$$

where κ is a positive spring constant. When κ is large enough, the displacement between $\vec{X}_k^e$ and $\vec{X}_k$ is negligible and the immersed boundary is approximately unmoved. Then, a rigid wall represented by $\vec{X}_k$ is simulated. It should be noted that although κ is preferred to be as large as possible, but large values of κ result in a stiff system which may subject to severe stability problem [16]. Although the IB method is only used to simulate a rigid wall here, it is obvious that more complicated boundaries, such as elastic and/or moving boundaries, can be simulated by suitably changing the mechanism of the "material properties".

In order to combine the desirable features of the LB and IB method, a first attempt to incorporate the IB method into the LBM/FDLBM framework was made by Feng and

Michaelides [26, 27]. In their work, the immersed points were used to simulate some moving inelastic particulates. An external force term which is due to the deformation of the particulate was computed by the penalty method [26] or the direct forcing scheme [27]. A similar idea was put forward by Niu et al. [28] and Strack and Cook [29]. Niu et al. [28] adopted a multi-relaxation collision LBM model and their forcing term was calculated by the momentum exchange method. On the other hand, Strack and Cook [29] applied a similar concept to treat problems with a moving boundary in 2-D and 3-D flows.

To implement the IB method into the FDLBM, the additional difficulty is to recover the NS equations with an external body force included. In previous work [26–29], an additional collision function is required to calculate the density distribution function f_α to account for the forcing function of the immersed boundary points. In the present scheme, the procedure of including an external body force has already been discussed in the formulation for cylindrical coordinates. Consequently, the extra work needed to perform here is to modify the distribution function g_α to account for the forcing function of the immersed boundary points in addition to that introduced by the cylindrical coordinates. The calculation procedures for f_α remain unchanged. This is a major difference between the present FDLBM/IB and other proposed LBM/IB methods reported in the literature [26–29]. The coefficients in Eq. (2.10b)-(2.10d) are thus modified to read

$$A_0=0, \qquad A_1=\frac{\rho v}{4y}, \qquad A_2=0, \tag{3.5a}$$

$$Ax_1=\frac{1}{2\sigma^2 y}\left(\rho uv-\tau_{xy}\right)+\frac{F_x^{ib}}{2\sigma^2}, \qquad Ax_2=0, \tag{3.5b}$$

$$Ay_1=\frac{1}{2\sigma^2 y}\left(\rho v^2-\tau_{yy}\right)+\frac{F_y^{ib}}{2\sigma^2}, \qquad Ay_2=0. \tag{3.5c}$$

As pointed out by Shu et al. [30], most IB methods use the restoring force technique; therefore, some streamlines may pass through the solid body because the non-slip condition is only approximately satisfied. To avoid this drawback, a new proposal called immersed boundary velocity correction method was put forward in [30]. In this method, the fractional step technique was used to directly enforce the non-slip boundary condition. Since no body force is involved in the prediction step, which is solved using LBM, it is not necessary to modify the lattice Boltzmann equation. The present FDLBM/IB also suffers from streamline leakage, much like most of the IB methods examined; however, it could be improved by adopting the immersed boundary velocity correction method. In this paper, the primary objective is to implement the IB into the present FDLBM, therefore, the relatively simple and well-established penalty method is attempted first.

3.1 Validation of the FDLBM/IB scheme

The FDLBM/IB scheme is validated against a known solution. A 2-D driven cavity flow with a Gaussian profile bed is chosen as an example. In this validating example, (x,y)

are respectively the horizontal and vertical coordinates and (u,v) are the horizontal and vertical velocity components along x and y, respectively. The cavity bed geometry is described by a Gaussian profile, i.e.,

$$h(x)=0.2\exp\left[-\frac{1}{2}\left(\frac{x-0.5}{0.1}\right)^2\right]. \tag{3.6}$$

With a Gaussian profile bed, a conformal grid can be generated for the FDLBM simulation without having to adopt the IB method. This way, the FDLBM/IB solution can be compared with the FDLBM simulation obtained using the conformal grid; thus allowing the accuracy of the IB method to be assessed directly.

Altogether, four different cases are investigated; the schematic diagrams of these cases are shown in Fig. 2. The computational domain is bounded by $0\leq(x,y)\leq 1$ with the upper wall ($y=1$) moving at velocity U and the physical parameters are specified as $\rho=1$, $U=1$, Re$=100$. In Case A and B, the bed profile is located at the bottom and slightly away from the bottom of the computational domain, respectively. Case C and D are similar to Case B except that the bottom of the computational domain is not stationary; instead, it is driven to the right ($U=1$) for case C and to the left ($U=-1$) for Case D. These four cases are chosen to check the effectiveness of the IB points as a no-slip wall. The equilibrium locations of the IB points are set as

$$\vec{X}_k^e=(x_k,h(x_k)), \tag{3.7}$$

where $x_k=(k-1)\Delta x$ and $k=1,\cdots,N$. The numerical parameters are defined by $\Delta x=\Delta y=0.01$, $\Delta t=0.0001$, $N=100$, $c=1$, $\kappa=10000$, and a Lax-Wendroff scheme is employed for the discretization of the advective term in Eq. (2.6). As an illustrative example, the streamline of the flow in Case A is plotted in Fig. 3; streamline plots of the other three cases are very similar and are not shown. Three characteristic vortexes are clearly displayed. It should be noted that the region between the immersed boundary and the computational boundary (arrow pointing) does not have any physical meaning; thus the computational resources seem wasted. However, one of the advantages of the FDLBM/IB is that it solves the equation locally; such waste of computational resource can be minimized by reducing the computational domain.

The results deduced from the FDLBM/IB scheme are compared with those given by a conformal grid. In the latter case, all spatial derivatives including the Jacobian in the grid transformation are discretized using a 2*nd* order central difference scheme, and the conservation of mass is ensured by using the artificial compressibility method of [31,32]. The numerical parameters are given by $\Delta x=\Delta y=0.01$, $\Delta t=0.0001$, which is the same as those of the FDLBM/IB case, and the grid is transformed by

$$x_p=x, \qquad y_p=y+h(1-y), \tag{3.8}$$

where (x,y) and (x_p,y_p) are, respectively, the coordinates in the computational and physical domain. Very good agreement between the calculated horizontal (u) and vertical

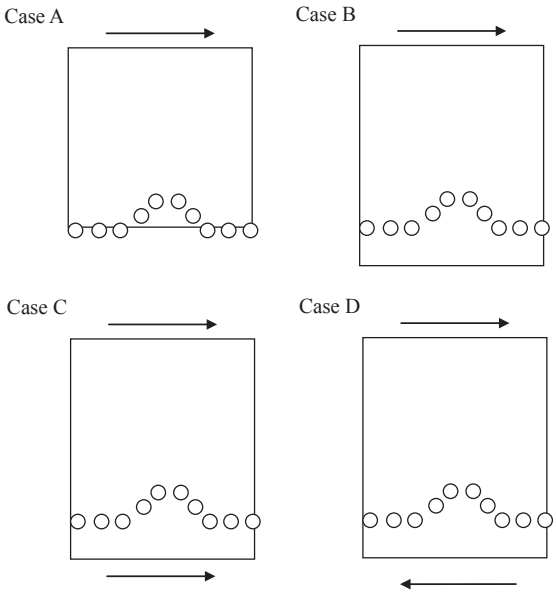

Figure 2: Schematics for the four driven cavity flow cases attempted by the FDLBM/IB method.

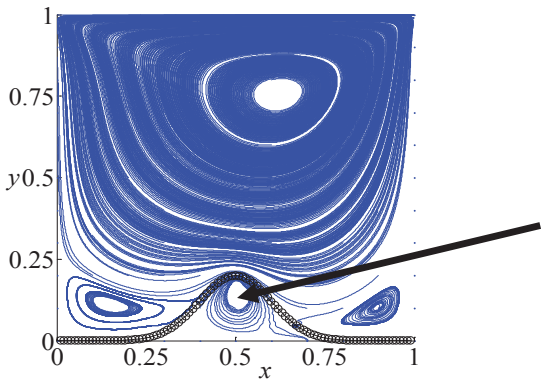

Figure 3: Streamline plot calculated using the FDLBM/IB method; symbol 'o' are the immersed boundary points at location $\vec{X}_k$, deviation of their location with $\vec{X}_k^e$ is insignificant.

(v) velocities at three different y locations is shown in Fig. 4. The solid line is the result calculated using conformal gird, while the symbols 'x', 'o', '∇', '$\triangle$' are the FDLBM/IB results for Case A, B, C, D, respectively. In Fig. 4, it should be noted that only the domains above $y \geq 0.008$, $y \geq 0.2$ and $y \geq 0.008$, for $x = 0.25$, $x = 0.5$, $x = 0.75$, respectively, are physically meaningful. All FDLBM/IB results are in excellent agreement with those calculated using conformal girds. It shows that the IB method simulates the no slip condition effectively and the calculation of the physically meaningful regions is basically unaffected by the artificial flow in the region bounded by the Gaussian profile and the cavity bottom.

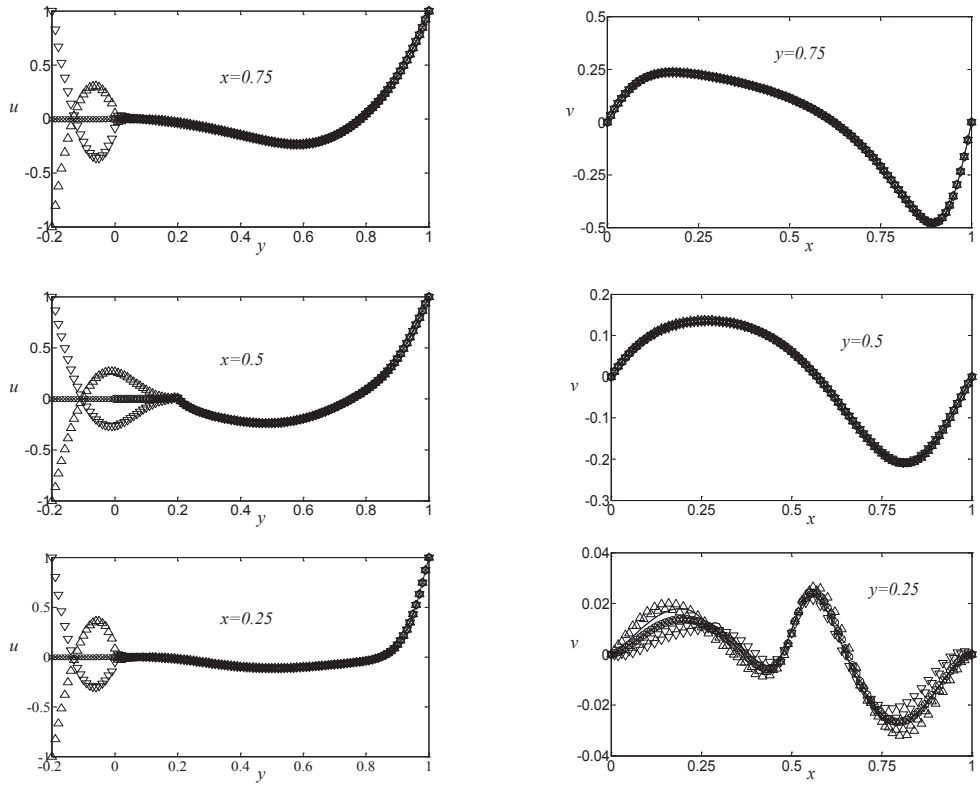

Figure 4: Distribution of the u and v velocity along y direction: "—" calculated using conformal grids; symbols 'x', 'o', '∇', '$\triangle$' represent results for Case A, B, C and D, respectively.

For the region close to the IB points (see the plot of y=0.25 in Fig. 4), the accuracy (first order only, i.e. $\mathcal{O}(\Delta x)$) is not as good as that of the region outside. It is because the discrete delta function inherent in the IB method smoothed out the sharp delta function resulting in an inability to provide a sharp representation near the IB points [24]. Anyway, the overall accuracy retains second order in space outside this small region.

4 FDLBM/IB simulation of model blood flows

Simulations for the various stenotic artery models with Newtonian and non-Newtonian (CY model) fluids over a wide range of Re are performed using FDLBM/IB. A rectangular computational domain of $-(10+X_0) \leq x \leq L$ and $0 \leq y \leq 1$ is used. It is noted that all the length scales are normalized by the radius $\hat{R}_0$ of the unconstricted tube. The inlet is located at 10 radii upstream of the start of the constriction, which is far enough to assure that the flow pattern is independent of the inlet position. The outlet is placed far enough downstream to allow the development of the characteristic separation pattern

and Poiseuille flow. The exact location of the computational outlet, L, should be determined case by case. In addition, an absorbing boundary treatment [33] is applied at the region near the outlet to ensure that any reflective waves, if present, are minimized. After every iteration step, the following absorbing boundary treatment is applied,

$$u = u_0 - \Delta t \kappa_d (u_0 - u_d), \qquad v = v_0 - \Delta t \kappa_d (v_0 - v_d), \tag{4.1}$$

where (u_0, v_0) is the flow velocity calculated immediately after each iteration, (u_d, v_d) is the expected Poiseuille flow at the outlet as defined by Eq. (2.4), Δt is the step size for the pseudo-time, and κ_d is a damping coefficient defined as

$$\kappa_d = \begin{cases} \sigma_d \left[\frac{x-(L-L_d)}{L_d} \right]^2, & x > L - L_d, \\ 0, & x \le L - L_d, \end{cases} \tag{4.2}$$

where L_d is the length of the damping region and σ_d is a damping factor. The settings $L_d = 10$, $\sigma d = 10$ are found to give satisfactory and effective results for all cases attempted here. The Newtonian cases are presented first; this is followed by a discussion of the non-Newtonian fluid flow cases.

4.1 Newtonian fluid

The number of model blood flow cases attempted in this section is summarized in Table 1. For ease of comparison, model M0, M1, M2 and M3 are exactly the same as those studied by Deshpande et al. [34]. Three more models, M02 and M04, for area reduction of 75%, and M31 for area reduction of 89%, are added in order to gain a more complete picture of the effect of area reduction and length of occlusion. Furthermore, they could facilitate a better comparison of the present approach with previous numerical methods.

Table 1: Geometry of constriction models and Re range investigated.

Model	α_1	X_0	Area Reduction	Range of Re Calculated
M0	0.500	1	75%	0-200
M02	0.500	2	75%	0-200
M04	0.500	4	75%	0-200
M1	0.333	4	56%	0-900
M2	0.667	4	89%	0-150
M3	0.667	2	89%	0-100
M31	0.667	1	89%	0-90

The streamline and vorticity plots for the M3 case with Re=50 are shown in Figs. 5(a) and 5(b), where the numerical parameters are set at $\Delta t = 10^{-4}$, $\Delta x = 0.05$, $\Delta y = 0.025$, $c = 4$, $L = 88$, $N = 100$, $\kappa = 100000$. For illustration purposes, only the plots of the M3 case with Re=50 are shown because the flow patterns for all other cases are similar. In all

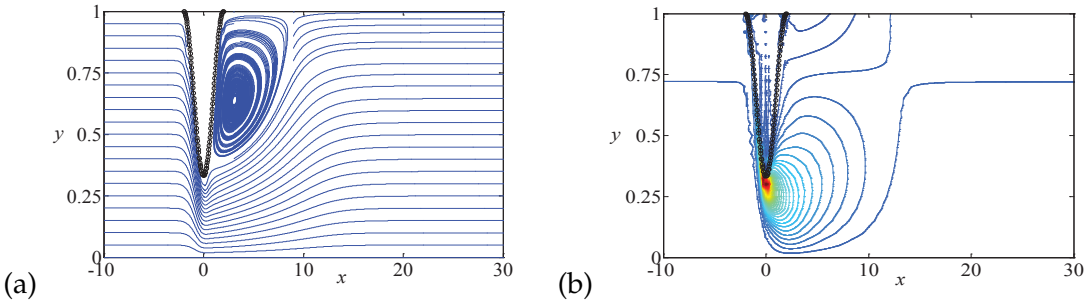

Figure 5: Streamline (a) and vorticity (b) plots for model M3 at Re=50; 'o', immersed boundary points (the area inside the immersed boundary should be ignored).

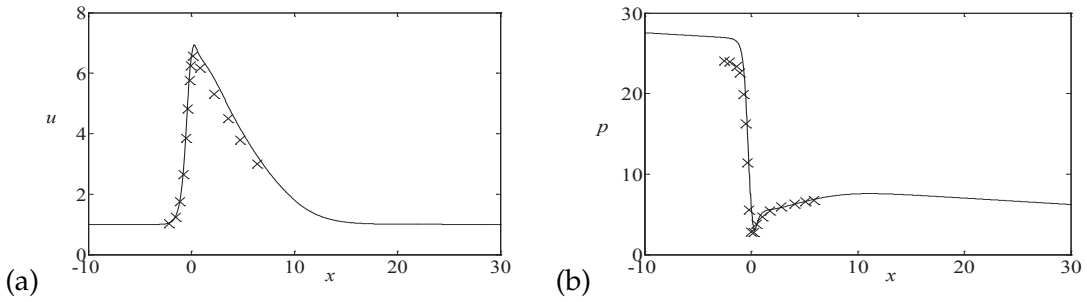

Figure 6: Axial velocity (a) and pressure (b) distribution at centerline for model M3 at Re=50; "—" FDLBM/IB calculation, "x" numerical result from Deshpande et al. [34].

cases calculated, only one recirculation region is observed downstream of the constriction when Re is 50 or larger. However, the size of the recirculation region is found to increase with Re. It should be noted that in these plots (Figs. 5(a) and 5(b)), the area inside the immersed boundary should be ignored. Distribution of the axial velocity and pressure at the centerline along the axial direction are shown in Figs. 6(a) and 6(b), where the data of [34] are also plotted for comparison. The FDLBM/IB results are in good agreement with those obtained by Deshpande et al. [34].

4.2 Non-Newtonian fluid (CY model)

In this section, the ability of the scheme to simulate non-Newtonian fluid flow through constricted tube is demonstrated. Again, the constriction models treated in the Newtonian fluid flow cases are considered here. In these simulations, the only difference between the current cases and those of the Newtonian fluid flow cases is in the viscosity model. For blood flow modeling, the power law model, Casson's model, and the Carreau-Yasuda (CY) model are the most popular among those used to replicate the shear thinning phenomena of blood flows [12, 35]. Experiments on blood rheology show that a yield stress is required for blood at rest to start flowing. However, the power law

model [35] does not take this characteristic feature into account. On the other hand, Casson's model takes this behavior into account; however, it is only valid for a small range of shear rate. According to Fung [36], Casson's model is only valid for blood with shear rates smaller than $10s^{-1}$ and hematocrit less than 40%. Also, the determination of yield stress in the equation is questionable [12]. The CY model takes this feature into account in its formulation; therefore, it is adopted in this section to investigate the shear thinning effect of blood on its flow in stenotic arteries. Experimental data of this model for a blood analog fluid can be found in Gijsen et al. [37]. In the CY model, non-Newtonian effect is reflected by a non-constant viscosity and, just as in Newtonian fluid, the stress tensor is written as,

$$\hat{\tau}_{ij}=\hat{\mu}\hat{\dot{\gamma}}_{ij}, \tag{4.3}$$

where the shear rate is

$$\hat{\dot{\gamma}}_{ij}=\frac{\partial\hat{u}_i}{\partial\hat{x}_j}+\frac{\partial\hat{u}_j}{\partial\hat{x}_i}. \tag{4.4}$$

The viscosity in the CY model is dependent on the shear rate and can be written as

$$\frac{\hat{\mu}-\hat{\mu}_\infty}{\hat{\mu}_z-\hat{\mu}_\infty}=\left[1+\left(\hat{\lambda}\left|\hat{\dot{\gamma}}\right|\right)^a\right]^{\frac{n-1}{a}}, \tag{4.5}$$

where $\hat{\mu}_z$ and $\hat{\mu}_\infty$ are the viscosity at zero and infinite shear rate, respectively, $\hat{\lambda}$ is a characteristic viscoelastic time of the fluid, n and a are two empirical parameters obtained by experiment. Using the radius of the artery $\hat{R}_0$ as characteristic length, the maximum speed $\hat{U}_0$ in the artery as characteristic speed, and normalizing the viscosity by $\hat{\rho}_0\hat{U}_0\hat{R}_0$ and λ by $\hat{R}_0/\hat{U}_0$, the dimensionless form of Eq. (4.7) can be re-arranged to give an expression for the viscosity as

$$\mu=\frac{1}{\mathrm{Re}_\infty}+\left(\frac{1}{\mathrm{Re}_z}-\frac{1}{\mathrm{Re}_\infty}\right)\left[1+\left(\lambda|\dot{\gamma}|\right)^a\right]^{\frac{n-1}{a}}. \tag{4.6}$$

The scalar measure of the rate of deformation $|\dot{\gamma}|$ is defined as [38]

$$\begin{aligned}|\dot{\gamma}|&=\sqrt{\frac{1}{2}\sum_i\sum_j\dot{\gamma}_{ij}\dot{\gamma}_{ji}}\\&=\sqrt{2\left(\frac{\partial u}{\partial x}\right)^2+\left(\frac{\partial u}{\partial y}+\frac{\partial v}{\partial x}\right)^2+2\left(\frac{\partial v}{\partial y}\right)^2}\qquad\text{for 2D,}\end{aligned} \tag{4.7}$$

and the two specific Reynolds numbers corresponding to the viscosity at zero ($\hat{\mu}_z$) and infinite ($\hat{\mu}_\infty$) shear rate are defined as

$$\mathrm{Re}_z=\frac{\hat{\rho}_0\hat{U}_0\hat{R}_0}{\hat{\mu}_z},\qquad \mathrm{Re}_\infty=\frac{\hat{\rho}_0\hat{U}_0\hat{R}_0}{\hat{\mu}_\infty}. \tag{4.8}$$

The experimental data obtained by Gijsen et al. [37] for a CY model to fit a blood analog fluid was $\hat{\mu}_z$=0.022Pa/s, $\hat{\mu}_\infty$=0.0022Pa/s, a=0.644, n=0.392, and $\hat{\lambda}$=0.110s. Also, setting the density of blood as 1050kg/m^3 [39] and using the typical blood flow data suggested in [21], i.e. $\hat{R}_0 = 2$mm, $\hat{U}_0 = 0.2653$m/s, the dimensionless physical parameters become $\mathrm{Re}_z = 25.324$, $\mathrm{Re}_\infty = 253.24$ and $\lambda = 14.59$.

The constriction models investigated previously are calculated again assuming a non-Newtonian fluid given by the CY model with physical parameters as stated above. The upstream condition for the non-Newtonian fluid flow is determined as follows. First, the velocity profile of the fully developed flow for the CY model is calculated using the Newtonian parabolic profile, Eq. (2.4), as the driving upstream condition. Second, after a steady, fully developed flow profile with the CY model has been obtained, it is used as the upstream boundary condition for the simulation of the constricted pipe flow with different constriction models. The flow pattern thus obtained for a non-Newtonian fluid (CY model) is very similar to that of the Newtonian fluid, i.e., only one flow separation region is observed downstream of the constriction.

Table 2 compares certain important flow characteristics, such as the reattachment location l_r, the minimum vorticity along the upper wall after the constriction $\omega_{\min}$, and the maximum vorticity over the whole domain $\omega_{\max}$, deduced from the Newtonian and non-Newtonian (CY model) fluid flow at different Re for constriction model M3. The reattachment location is identified as the position where the vorticity vanishes along the upper wall after the constriction. The maximum and the minimum vorticities calculated by the CY model do not exceed the bounds of the Newtonian calculations at Re = 105. Also, the CY model simulation yields a longer reattachment length compared to all Newtonian cases investigated. These results show that vorticity is more quickly dispersed by the non-Newtonian fluid (CY model) investigated.

Table 2: Comparison of certain important characteristics between Newtonian and non-Newtonian (CY model) fluid at different Re for model M3.

	Newtonian				Non-Newtonian
	Re = 15	Re = 30	Re = 50	Re = 105	CY Model
l_r	2.7	5.45	8.95	18.65	20.75
$\omega_{\min}$	−0.7027	−2.229	−2.6970	−3.4465	−1.9984
$\omega_{\max}$	70.8975	81.9791	82.9952	112.7575	86.7025

The non-Newtonian shear thinning effect can be further visualized from the contour plots of the normalized viscosity for constriction model M3 as shown in Fig. 7. The normalized viscosity is in fact the reciprocal of the 'local' Re, i.e. $\mu = \hat{\mu}_0/\hat{\rho}_0\hat{U}_0\hat{R}_0 = 1/\mathrm{Re}$. It should be noted that the Re defined here is not exactly a local one because only the viscosity is local; the reference parameters for length and velocity are still $\hat{R}_0$ and $\hat{U}_0$, respectively. For the Newtonian fluid, it is observed that numerical calculations become more difficult when Re exceeds a hundred because flow transition to turbulence is beginning to occur. However, for non-Newtonian fluid (CY model), the 'local' Re may increase

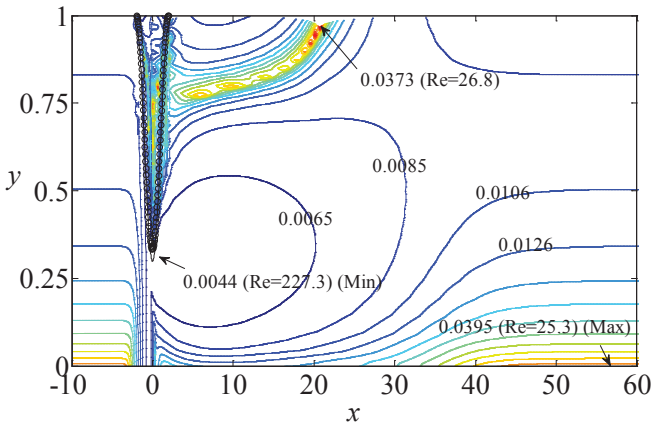

Figure 7: Normalized viscosity (reciprocal of the 'local' Reynolds number) contour for model M3 derived from non-Newtonian fluid (CY model) a; 'o', immersed boundary points. There are 64 equally distributed contour lines, and the maximum and minimum bounds are 0.0395 and 0.0044.

to two hundred when the shear rate is approaching infinite, but the flow is still laminar and a stable numerical solution is obtained. Thus, it appears that shear thinning tends to promote flow stabilization, or to delay transition to turbulence.

5 Scaling laws for pressure drop and wall shear stress

Considerable research has been carried out to identify factors causing atherosclerosis and related cardiovascular diseases [40–42]. Atherosclerosis tends to form and grow at certain locations of arteries (bifurcations, bending, etc.). The type of artery where plaque develops varies with each person. The exact mechanism of this entire process remains unresolved, but there has been increasing evidence that hemodynamics is closely related to intimal thickening, lipid deposition and endothelial adaptations, cell adhesion, elongation, and adaptation, thrombus development, and various cell behaviours under specific shear stress conditions. Blood pressure and wall stress have considerable effects on artery remodelling. High shear stress may damage normal endothelium; it may also activate platelets and cause platelets aggregation and thrombus formation. Consequently, there might be a high correlation between the development of atherosclerosis and abnormal wall shear stress [43].

Having verified the FDLBM/IB simulations with the experimental measurements of Deshpande et al. [34], the next step is to derive empirical relations for the pressure drop and wall shear stress using the Newtonian fluid flow results obtained from the FDLBM/IB simulations, and compared the relations thus deduced with those derived from experimental measurements. This is followed by an assessment of the effect of non-Newtonian fluid (CY model) on the pressure drop and wall shear behavior.

5.1 Scaling law for pressure drop

The experimental data of [44] was measured by transducers connected to wall taps located at ± 16 radii from the plane of minimum constriction. For comparison purpose, the same scaling is used in the present analysis. It should be noted that they used the mean velocity $\hat{U}_m$, instead of the maximum velocity $\hat{U}_0$ of the Poiseuille flow to normalize the velocity, which is different from the present study. Also, the inlet of the present calculation is located at 10 radii upstream of the start of the constriction, which is smaller than 16 radii specified in [44]. As a result, an extrapolation assuming Poiseuille flow is used to obtain the pressure drop. A grid refinement analysis is carried out on model M0. From existing literature data, the velocity gradient along the y-axis is expected to be more significant than that along the x-axis, so gird dependence is investigated by varying Δy while keeping Δx constant at 0.05. In Fig. 8, the pressure drop is plotted against Re at different Δy. A converging limit is observed in Fig. 9 in which only the case of $\mathrm{Re}=7.5$ is shown. It should be pointed out that a finer grid is desirable especially for cases with higher Re (see Fig. 8). In order to save computing time, all calculations presented below use $y=0.025$, which only deviates a few percent from the finer grid ($\Delta y=0.02$) result (Fig. 8).

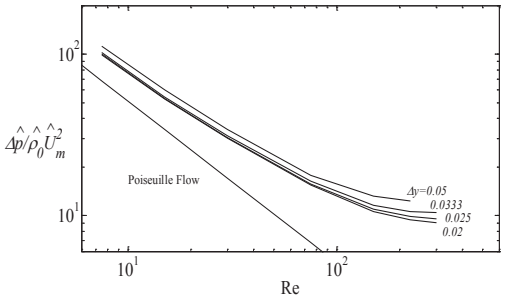

Figure 8: Pressure drop versus Re at different Δy for model M0 (logarithmic scale).

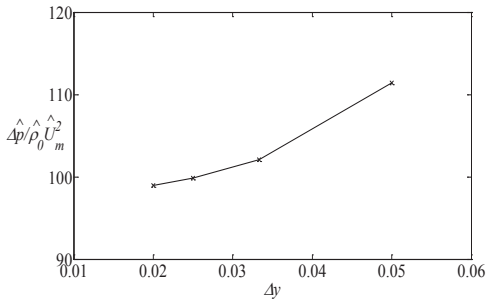

Figure 9: Pressure drop versus Δy at $\mathrm{Re}=7.5$ for Model M0.

Fig. 6 of Deshpande et al. [34] with $\Delta\hat{p}/\hat{\rho}_0\hat{U}_m^2$ vs Re was replicated in Fig. 10. Included for comparison are the experimental data of [44] and the present FDLBM/IB results. At very small Re, all curves are parallel to that given by a Poiseuille flow. The slope of the curve increases with Re; implying that the inertia term is becoming more important than the viscous term. The pressure drop eventually becomes independent of Re, at which point the flow begins its transition to turbulence [34,44]. The present mathematical models and [34] do not account for transition to turbulence; therefore, it is not surprising that the modeling results deviate from experimental data [44] at high Re.

Young and Tsai [44] proposed an empirical formula for the pressure drop as

$$\frac{\Delta\hat{p}}{\hat{\rho}_0\hat{U}_m^2}=\frac{K_v}{\mathrm{Re}}+\frac{K_t}{2}A^2, \tag{5.1}$$

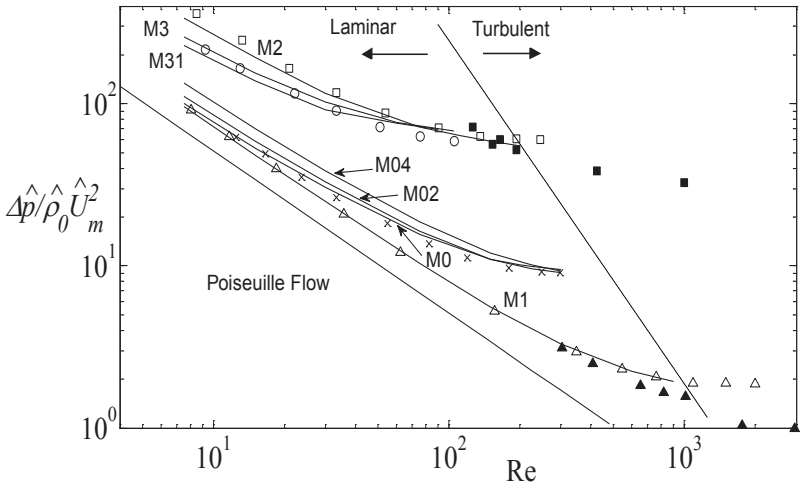

Figure 10: Comparison of pressure drop between ± 16 radii from plane of minimum constriction with previous numerical [34] and experimental [44] data: '—' FDLBM/IB results; $\times$, $\triangle$, $\square$ and $\circ$ are data from [34] for model M0, M1, M2, M3, respectively; ▲ and ■ are data from [44] for model M1 and M2, respectively.

where A is the area reduction, K_v and K_t are two geometry dependent coefficients to be determined. They argued that, as a first attempt, $\Delta\hat{p}$ can be approximated by the sum of the losses due to viscous effect (1*st* term on RHS) and turbulence (2*nd* term on RHS). Although the present study assumes laminar flow, the results show that $\Delta\hat{p}$ is essentially proportional to 1/Re; hence, Eq. (5.1) is still applicable for the present study.

It is observed that in some models, the position of 16 radii after the plane of minimum constriction as a pressure measurement point may not be long enough for pressure recovery to the Poiseuille flow behavior (e.g. see Fig. 6). It would be more desirable to examine only the $\Delta\hat{p}$ due to the constriction and ignore the distance between measurement points. Therefore, another pressure drop given by $\delta p = \delta\hat{p}/\hat{\rho}_0\hat{U}_0^2$ is proposed; this δp is defined as the difference between the pressure far enough downstream of the constriction and the pressure at the same location calculated without constriction (Poiseuille flow). It is assumed that δp can be expressed as

$$\delta p = \frac{\delta\hat{p}}{\hat{\rho}_0\hat{U}_0^2} = f(X_0, A, Re) = \frac{K'_v}{\mathrm{Re}} + K'_t. \tag{5.2}$$

The values of the coefficients determined from the present analysis are given in Table 3. Both coefficients are dependent on the geometry of the constriction. For the series of models with the same area reduction, K'_t essentially remains unchanged; thus showing that assuming K'_t to be solely dependent on A, as suggested in Eq. (5.1), is a good approximation. From the series of models with the same area reduction (for $A = 75\%$, Models M0, M02 & M04; for $A = 89\%$, Models M31, M3 & M2), K'_v is found to increase linearly with X_0 (see Table 3).

Table 3: Pressure drop coefficients for Eq. (5.2).

Model	X_0	A	K'_v	K'_t	R^2-value
M1	4	56%	49.91	0.1743	0.9999
M0	1	75%	48.84	1.4975	0.9974
M02	2	75%	70.675	1.3724	0.9985
M04	4	75%	113.85	1.3486	0.9991
M31	1	89%	199.44	12.957	0.9970
M3	2	89%	258.83	12.750	0.9999
M2	4	89%	429.04	10.116	0.9993

5.2 Scaling law for maximum wall shear stress

Results for wall shear stress from existing literature were mostly approximated by the assumption that it is proportional to the vorticity [21, 22, 34], because they solved the stream-function-vorticity form of the NS equation. The use of wall vorticity on a curved surface to approximate shear rate requires the assumption that

$$\frac{\partial u_n}{\partial x_s} \ll \frac{\partial u_s}{\partial x_n}, \tag{5.3}$$

where the subscripts 'n' and 's' denote the normal and tangential direction of the surface. However, the validity of this assumption cannot be ascertained. In the present calculation, the primitive variables are solved directly. The wall shear stress can be calculated from the shear stress tensor by interpolation along the wall profile. It is known that the discrete delta function inherent in the IB method smoothed out the sharp delta function resulting in an inability to provide a sharp representation near the IB points [24]. Consequently, the results at the position exactly along the IB obtained simply by interpolation will look "smeared" and may not be reliable. Therefore, the following two extrapolation methods are attempted in order to find the more correct wall shear stress. The stress tensor at the wall is found either by

$$\tau_{i,j=M} = \left(4\tau_{i,j=M-1} - \tau_{i,j=M-2}\right)/3, \tag{5.4a}$$

or

$$\tau_{i,j=M} = 2\tau_{i,j=M-1} - \tau_{i,j=M-2}, \tag{5.4b}$$

where $\tau_{i,j}$ stands for the components of the stress tensor, τ_{xx}, τ_{xy} and τ_{yy}, at position indexed by i and j along the wall profile and its offset as shown in Fig. 11. For the position $j = M$, it represents the wall profile, $R(x)$ in Eq. (2.5). The positions $j = M-1$ and $j = M-2$ represent the profile offset from the wall vertically (in y-direction) with Δy and $2\Delta y$, respectively. The wall shear stress $\tau_{i,j=M-1}$ and $\tau_{i,j=M-2}$ are found by interpolation of the components of the stress tensor. Using Eq. (5.4a), the gradients of the stress components, which are approximated by the second order one-side finite difference discretization, are

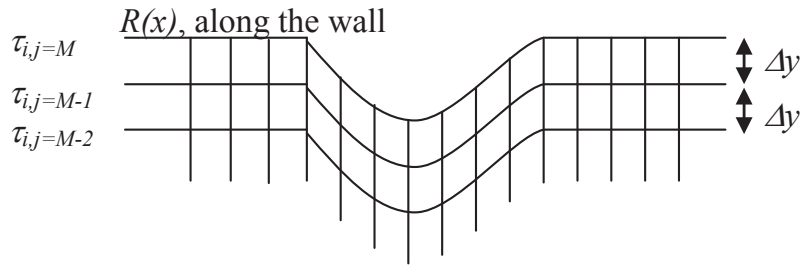

Figure 11: Schematic of IB to illustrate how wall shear stress is determined by extrapolation.

assumed zero along the y-direction. As for Eq. (5.4b), it is a simple extrapolation method used in [45]. After the required components of the stress tensor along the wall are known, the wall shear stress is given by the dot product with the tangential and normal vectors of the wall profile.

Siegel et al. [21] obtained a scaling law for the maximum wall shear rate, which is, in normalized form, proportional to the wall shear stress by a factor of 1/Re. They found that the maximum shear rate was linearly proportional to the square root of Re. Instead of fixing the power exponent for the Re as 0.5, a more general empirical formula for data fitting is suggested,

$$\tau_{w,m} = f(X_0, A, \mathrm{Re}) = a\mathrm{Re}^{-n} + b, \tag{5.5}$$

where $\tau_{w,m}$ is the maximum wall shear stress normalized by $\hat{\rho}_0 \hat{U}_0^2$. The values of the coefficients as determined from the present analysis are presented in Tables 4 and 5. All coefficients a, b, n are constriction geometry dependent. The results from both extrapolation methods, Eqs. (5.4a) and (5.4b), are very similar. Therefore, the "smearing effect" due to the immersed boundary method is not very significant in the present study. From the present analysis, the power exponent, n, is generally greater than 0.5 and it decreases when the area reduction increases.

Table 4: Wall shear stress coefficients for Eq. (5.5) according to Eq. (5.4a).

Model	X_0	A	a	b	n	R^2-value
M1	4	56%	5.9611	0.0164	0.95	0.9999
M0	1	75%	12.910	-0.0010	0.85	0.9998
M02	2	75%	11.026	0.0317	0.85	0.9998
M04	4	75%	8.6781	0.0398	0.85	1.0000
M31	1	89%	28.543	-0.2910	0.75	0.9999
M3	2	89%	31.254	-0.3725	0.70	0.9997
M2	4	89%	17.438	-0.2699	0.60	0.9993

Table 5: Wall shear stress coefficients for Eq. (5.5) according to Eq. (5.4b).

Model	X_0	A	a	b	n	R^2-value
M1	4	56%	6.0885	0.0214	0.95	0.9999
M0	1	75%	12.839	-0.0115	0.85	0.9997
M02	2	75%	11.571	0.0373	0.85	0.9996
M04	4	75%	8.8272	0.0578	0.85	1.0000
M31	1	89%	22.913	-0.2097	0.75	0.9997
M3	2	89%	33.458	-0.3393	0.70	0.9968
M2	4	89%	17.744	-0.1142	0.60	0.9996

5.3 Non-Newtonian fluid (CY model) effect

Table 6 shows the result of the pressure drop of non-Newtonian fluid (CY model) against different occlusion models. The pressure drop δp is again estimated using the method discussed in previous section under scaling law for pressure drop. Similar to the Newtonian case, δp is mainly determined by the area reduction A. In order to compare the shear thinning effect of the CY model with the Newtonian model, the empirical formulae of δp for Newtonian fluid together with the results of the CY model are plotted in Figs. 12-14. Since the CY model covers a range of viscosity, resulting in a range of Re (ranging from $\mathrm{Re}_z = 25.324$ to $\mathrm{Re}_\infty = 253.24$), the non-Newtonian fluid results are plotted as a horizontal line in the figures. It should be noted that the horizontal line for the CY model doesn't mean that the pressure drop is independent on the 'local' Re, or the normalized viscosity. On the other hand, the pressure drop of the CY model is dependent on a range of Re and only one horizontal line is plotted for each case because only one range of Re is calculated for each constriction case. It is shown that the pressure drop of the CY model is in general smaller than that deduced from the Newtonian model, which implies that a Newtonian fluid assumption tends to overestimate the pressure drop in blood flow simulation.

Table 6: Pressure drop derived from non-Newtonian fluid (CY model).

Model	X_0	A	δp
M1	4	56%	0.4351
M0	1	75%	1.5411
M02	2	75%	1.4959
M04	4	75%	1.7185
M31	1	89%	11.5616
M3	2	89%	9.4820
M2	4	89%	8.0742

The non-Newtonian effect on the maximum wall shear stress is investigated also. Table 7 shows the results obtained using extrapolation methods stated in Eqs. (5.4a) and (5.4b). Again, it can be seen that the result is mainly determined by the area reduction

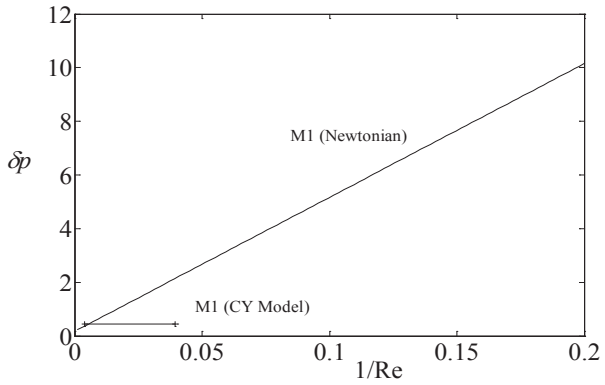

Figure 12: Comparison of pressure drop between Newtonian and non-Newtonian (CY model) fluid for model M1 ($A=56\%$, $X_0=4$).

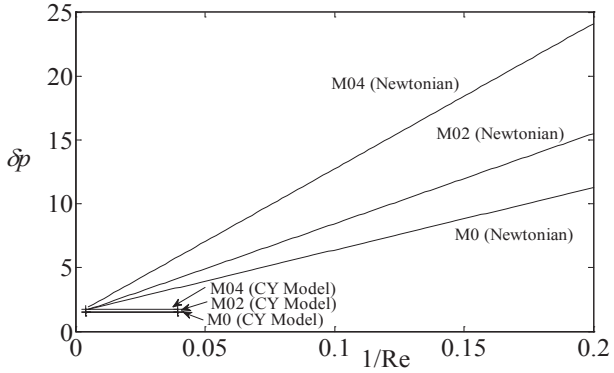

Figure 13: Comparison of pressure drop between Newtonian and non-Newtonian (CY model) fluid for $A=75\%$; model M0 ($X_0=1$), M02 ($X_0=2$) and M04 ($X_0=4$).

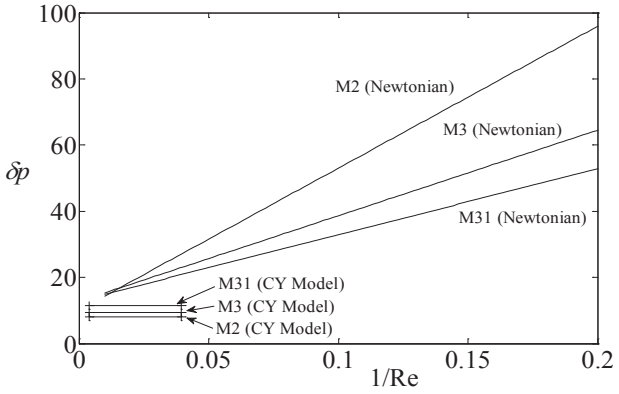

Figure 14: Comparison of pressure drop between Newtonian and non-Newtonian (CY model) fluid for $A=89\%$; model M2 ($X_0=4$), M3 ($X_0=2$) and M31 ($X_0=1$).

Table 7: Maximum wall shear stress derived from non-Newtonian fluid (CY model).

Model	X_0	A	Maximum wall shear stress from Eq. (5.4a)	Eq. (5.4b)
M1	4	56%	0.0629	0.0683
M0	1	75%	0.1188	0.1025
M02	2	75%	0.1413	0.1492
M04	4	75%	0.1375	0.1576
M31	1	89%	0.3220	0.3125
M3	2	89%	0.3670	0.4225
M2	4	89%	0.3178	0.4009

A when compares to the effect of X_0. The comparison between the CY model of non-Newtonian fluid and Newtonian fluid flow for constriction model with $X_0=4$ is shown in Fig. 15 and the maximum shear stress is found by the extrapolation method given in Eq. (5.4a). Similar to the δp results, the maximum wall shear stress is also overestimated by assuming blood to be modeled by a Newtonian fluid. This implies that an appropriate non-Newtonian fluid model for blood should be at least one that accounts for shear thinning, such as the CY model.

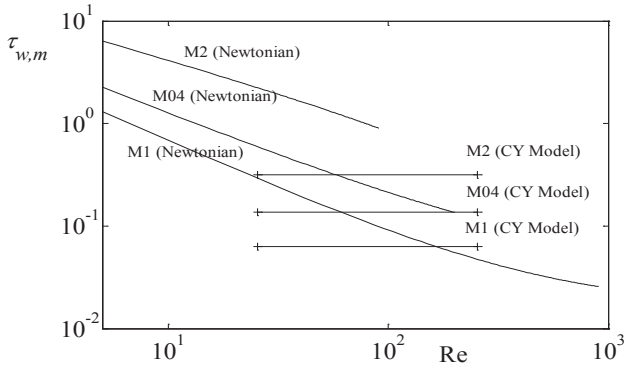

Figure 15: Comparison of maximum wall shear stress using extrapolation in Eq. (5.4a) between Newtonian and non-Newtonian (CY model) fluid for $X_0=4$; model M2 ($A=89\%$), M04 ($A=75\%$) and M1 ($A=56\%$).

6 Conclusions

The FDLBM and the IB method have been successfully integrated to give the FDLBM/IB numerical scheme for model blood flow problems. The FDLBM/IB scheme has been validated against known numerical solution. Consequently, the FDLBM/IB scheme can be extended to treat axisymmetric flow through constricted tubes. The FDLBM is applicable for Newtonian and non-Newtonian fluids and is able to correctly replicate incompressible flow with constant density invoked for the whole flow field. In this paper, Newtonian

and non-Newtonian flow through constricted tubes with different constriction geometries is treated without numerical instability and with accuracy. These characteristics are most desirable for any solver used to simulate blood flows. Thus developed, the data of the FDLBM/IB simulations have been used to deduce scaling laws for pressure drop and wall shear stress in constricted tubes and the results are found to be in agreement with previous studies. If this FDLBM/IB scheme were to be truly applicable for real blood flow problems, its ability to simulate pulsating flow in a fully three-dimensional environment needs to be developed. In a companion paper [46], the ability of the FDLBM/IB scheme to simulate Newtonian and non-Newtonian pulsating flow in an axisymmetric blood vessel is reported. Extension of the unsteady FDLBM/IB to fully three-dimensional model blood flow problem where the vessel wall could be elastic is currently being attempted.

Acknowledgments

SCF gratefully acknowledges funding support in the form of a PhD studentship awarded him by the Hong Kong Polytechnic University. RMCS acknowledges support received as Co-PI from the NSF Grant CBET-0854411 awarded to New Mexico State University.

References

[1] Davies, M. J. and Thomas, A. C., 1985, Plaque Fissuring - The Cause of Acute Myocardial Infarction, Sudden Ischemic Death, and Crescendo Angina, British Heart Journal, 53(4), pp. 363-373.

[2] Fuster, V., Stein, B., Ambrose, J. A., Badimon, L., Badimon, J. J. and Chesebro, J. H., 1990, Atherosclerotic Plaque Rupture and Thrombosis, Circulation, Supplement II, 82(3), pp. II-47-II-59.

[3] Burke, A. P., Farb, A., Malcom, G. T., Liang, Y. H., Smialek, J. E. and Virmani, R., 1999, Plaque Rupture and Sudden Death Related to Exertion in Men with Coronary Artery Disease, Journal of the American Medical Association, 281(10), pp. 921-926.

[4] Chen, S. and Doolen, G. D., 1998, Lattice Boltzmann Method for Fluid Flows, Annual Review of Fluid Mechanics, 30, pp. 329-364.

[5] Wolf-Gladrow, D. A., 2000, Lattice-Gas Cellular Automata and Lattice Boltzmann Models: An Introduction, Chapter 5, Springer-Verlag.

[6] Sterling, J. D. and Chen, S., 1996, Stability Analysis of Lattice Boltzmann Methods, Journal of Computational Physics, 123(1), pp. 196-206.

[7] Wellein, G., Lammers, P., Hager, G., Donath, S. and Zeiser, T., 2005, Towards Optimal Performance for Lattice Boltzmann Applications on Terascale Computers, in Parallel Computational Fluid Dynamics: Theory and Applications (Editors: A. Deane et al.), Proceedings of the 2005 International Conference on Parallel Computational Fluid Dynamics, May 24-27, College Park, MD, USA, pp. 31-40.

[8] Wellein, G., Zeiser, T., Hager, G. and Donath S, 2006, On the Single Processor Performance for Simple Lattice Boltzmann Kernels, Computers and Fluids, 35, pp. 910-919.

[9] Krafczyk, M., Cerrolzaz, M., Schulz, M. and Rank, E., 1998, Analysis of 3D Transient Blood Flow Passing Through an Artificial Aortic Valve by Lattice-Boltzmann Methods, Journal of Biomechanics, 31(5), pp. 453-462.
[10] Ouared, R., Chopard, B., Stahl, B., R?fenacht, D. A., Yilmaz, H., and Courbebaisse, G., 2008, Thrombosis Modelling in Intracranial Aneurysms: A Lattice Boltzmann Numerical Algorithm, Computer Physics Communications, 179(1-3), pp. 128-131.
[11] Bernsdorf, J., Harrison, S. E., Smith, S. M., Lawford, P. V., and Hose, D. R., 2008, Applying the Lattice Boltzmann Technique to Biofluids: A Novel Approach to Simulate Blood Coagulation, Computers and Mathematics with Applications, 55(7), pp. 1408-1414.
[12] Wang, D., and Bernsdorf, J., 2009, Lattice Boltzmann Simulation of Steady Non-Newtonian Blood Flow in a 3D Generic Stenosis Case, Computer and Mathematics with Applications, 58(5), pp. 1030-1034.
[13] Chen, C., Chen, H, Freed, D., Shock, R., Staroselsky, I., Zhang, R., Co?kun, A. ?., Stone, P. H., and Feldman, C. L., 2006, Simulation of Blood Flow Using Extended Boltzmann Kinetic Approach, Physica A, 362(1), pp. 174-181.
[14] Boyd, J., Buick, J. M., Cosgrove, J. A., and Stansell, P., 2004, Application of the Lattice Boltzmann Method to Arterial Flow Simulation: Investigation of Boundary Conditions for Complex Arterial Geometries, Australasian Physical & Engineering Sciences in Medicine, 27(4), pp. 207-212.
[15] Peskin, C. S., 1977, Numerical Analysis of Blood Flow in the Heart, Journal of Computational Physics, 25(3), pp. 220-252.
[16] Mittal, R. and Iaccarino G., 2005, Immersed Boundary Methods, Annual Review of Fluid Mechanics, 37, pp. 239-261.
[17] Fu, S. C., Leung, W. W. F. and So, R. M. C., 2009, A Lattice Boltzmann Based Numerical Scheme for Microchannel Flows, Journal of Fluids Engineering, 131(August), Paper 081401(11 pages).
[18] Fu, S. C. and So, R. M. C., 2009, Modeled Boltzmann Equation and the Constant Density Assumption, AIAA Journal, 47(12), pp. 3038-3042.
[19] He, X. and Luo, L. S., 1997, Lattice Boltzmann Model for the Incompressible Navier-Stokes Equation, Journal of Statistical Physics, 88(3/4), pp. 927-944.
[20] Fu, S. C., So, R. M. C. and Leung, W. W. F., 2011, A Discrete Flux Scheme for Aerodynamic and Hydrodynamic Flows, Communications in Computational Physics 9(5), 1257-1283.
[21] Siegel, J. M., Markou, C. P., Ku, D. N. and Hanson, S. R., 1994, A Scaling Law for Wall Shear Rate through an Arterial Stenosis, Journal of Biomechanical Engineering, 116(4), pp. 446-451.
[22] Huang, H., Modi, V. J. and Seymour, B. R., 1995, Fluid Mechanics of Stenosed Arteries, International Journal of Engineering Science, 33(6), pp. 815-828.
[23] Fu, S. C., 2011, Numerical Simulation of Blood Flow in Stenotic Arteries, PhD thesis, Mechanical Engineering Department, The Hong Kong Polytechnic University, Hung Hom, Hong Kong.
[24] Beyer, R. P. and Leveque, R. J., 1992, Analysis of a One-Dimensional Model for the Immersed Boundary Method, SIAM Journal on Numerical Analysis, 29(2), pp. 332-364.
[25] Lai, M. C. and Peskin, C. S., 2000, An Immersed Boundary Method with Formal Second-Order Accuracy and Reduced Numerical Viscosity, Journal of Computational Physics, 160(2), pp. 705-719.
[26] Feng, Z. G. and Michaelides, E. E., 2004, The Immersed Boundary-lattice Boltzmann Method for Solving Fluid-particles Interaction Problems, Journal of Computational Physics, 195, pp. 602-628.

[27] Feng, Z. G. and Michaelides, E. E., 2005, Proteus: a Direct Forcing Method in the Simulations of Particulate Flows, Journal of Computational Physics, 202, pp. 20-51.
[28] Niu, X. D., Shu, C., Chew, Y. T. and Peng, Y., 2006, A Momentum Exchange-based Immersed Boundary-lattice Boltzmann Method for Simulating Incompressible Viscous Flows, Physics Letters A, 354, pp. 173-182.
[29] Strack, O. E. and Cook, B. K., 2007, Three-Dimensional Immersed Boundary Conditions for Moving Solids in the Lattice-Boltzmann Method, International Journal for Numerical Methods in Fluids, 55, pp.103-125.
[30] Shu, C., Liu, N. and Chew, Y. T., 2007, A Novel Immersed Boundary Velocity Correction-Lattice Boltzmann Method and Its application to Simulate Flow Past a Circular Cylinder, Journal of Computational Physics, 226, pp. 1607-1622.
[31] Chorin, A. J., 1967, A Numerical Method for Solving Incompressible Viscous Flow Problems, Journal of Computational Physics, 2, pp. 12-26.
[32] Tannehill, J. C., Anderson, D. A. and Pletcher, R. H., 1997, Computational Fluid Mechanics and Heat Transfer, 2nd ed., Taylor & Francis, Washington, D.C., Chap. 9, pp. 649-776.
[33] Kam, E. W. S., So, R. M. C., and Leung, R. C. K., 2007, Lattice Boltzamann Method Simulation of Aeroacoustics and Nonreflecting Boundary Conditions, AIAA Journal, 45(7), pp. 1703-1712.
[34] Deshpande, M. D., Giddens, D. P. and Mabon, R. F., 1976, Steady Laminar Flow Through Modeled Vascular Stenoses, Journal of Biomechanics, 9(4), pp. 165-174.
[35] Shibeshi, S. S and Collins, W. E., 2005, The Rheology of Blood Flow in a Branched Arterial System, Applied Rheology, 15(6), pp. 398-405.
[36] Fung, Y. C., 1993, Biomechanics: Mechanical Properties of Living Tissue, Springer-Verlag, Chap. 3.
[37] Gijsen, F. J. H., van de Vosse, F. N. and Janssen, J. D., 1999, The Influence of the Non-Newtonian Properties of Blood on the Flow in Large Arteries: Steady Flow in a Carotid Bifurcation Model, Journal of Biomechanics, 32, pp. 601-608.
[38] Bird, R. B., Armstrong, R. C. and Hassager, O., 1987, Dynamics of Polymeric Liquids, Vol. 1, 2nd ed., Wiley, New York, p. 171.
[39] Waite, G.N. 2009, Blood Components, in Medical Physiology, 3rd Edition, Rhoades, R. and Bell, D. (Eds). Lippincott Williams & Wilkings, U.S.A., Chap. 9, p. 171.
[40] Nerem, R. M., 1993, Haemodynamics and the Vascular Endothelium, ASME Journal of Biomechanical Engineering, 115(4B), pp. 510-514.
[41] Ku, D. N., 1997, Blood Flow in Arteries, Annual Review of Fluid Mechanics, 29, pp. 399-434.
[42] Wootton, D. M. and Ku, D. N., 1999, Fluid Mechanics of Vascular Systems, Diseases, and Thrombosis, Annual Review of Biomedical Engineering, 1, pp. 299-329.
[43] Giddens, D. P., Zarins, C. K., and Glagov, S., 1993, The Role of Fluid Mechanics in the Localization and Detection of Atherosclerosis, Journal of Biomechanical Engineering, 115(4B), pp. 588-594.
[44] Young, D. and Tsai, F., 1973, Flow Characteristics in Models of Arterial Stenoses - I. Steady flow, Journal of Biomechanics, 6(4), pp. 395-402.
[45] Anderson, J. D., 1995, Computational Fluid Dynamics: The Basics with Applications, McGraw-Hill, New York, Ch. 10, pp. 458-459.
[46] Fu, S. C., So, R. M. C. and Leung, W. W. F., 2013, A Lattice Boltzmann and Immersed Boundary Scheme for Model Blood Flow in Constricted Pipes: Part 2 - Pulsatile Flow, Communications in Computational Physics, 14(1), pp. 153-173.